ARTICLE

Bioactive $SrTiO_3$ Nanotube Arrays: Strontium Delivery Platform on Ti-Based Osteoporotic Bone Implants

Yunchang Xin,[†] Jiang Jiang,[†] Kaifu Huo,[†,‡,*] Tao Hu,[†] and Paul K. Chu[†,*]

[†]Department of Physics and Materials Science, City University of Hong Kong, Tat Chee Avenue, Kowloon, Hong Kong, China, and [‡]Hubei Province Key Laboratory of Ceramics and Refractories, School of Materials and Metallurgy, Wuhan University of Science and Technology, Wuhan 430081, China

ABSTRACT Development of strontium releasing implants capable of stimulating bone formation and inhibiting bone resorption is a desirable solution for curing osteoporosis. In this work, well-ordered $SrTiO_3$ nanotube arrays capable of Sr release at a slow rate and for a long time are successfully fabricated on titanium by simple hydrothermal treatment of anodized titania nanotubes. This surface architecture combines the functions of nanoscaled topography and Sr release to enhance osseointegration while at the same time leaving space for loading of other functional substances. *In vitro* experiments reveal that the $SrTiO_3$ nanotube arrays possess good biocompatibility and can induce precipitation of hydroxyapatite from simulated body fluids (SBF). This Ti-based implant with $SrTiO_3$ nanotube arrays is an ideal candidate for osteoporotic bone implants. The proposed method can also be extended to load other biologically useful elements such as Mg and Zn.

KEYWORDS: osteoporosis · $SrTiO_3$ nanotube arrays · strontium · bioactivity

Osteoporosis in the aging population and postmenopausal women often induces pathological fracture.[1] Low attachment and proliferation as well as decreased collagen and osteocalcin synthesis ability of osteoblasts in these patients negatively influence the osseointegration process of biomedical implants.[1] Their poor bone quality and higher osteoclastic activity also expedite loosening of replacement implants. Hence, the design of novel orthopedic implants capable of promoting bone formation and inhibiting bone resorption is urgent and of great importance.

There is increasing evidence that a suitable nanoscaled topography can significantly promote the osseoinduction ability of implants. Recently, a highly ordered titania nanotube array with high specific surface area and surface energy has been fabricated by anodization of pure titanium plates or titanium alloys.[2−11] *In vitro* and *in vivo* experiments have revealed that this nanoscaled topography can guide enhanced cellular migration on the surface, promote differentiation and matrix production of bone cells, and enhance both short- and long-term osseointegration.[5,8,12,13] The hollow tubes also constitute an excellent platform for drug delivery carriers and immobilization of various functional substances such as antimicrobials, trace elements, growth factors, and so on.[7,14−18] Strontium ranelate is widely used clinically for treatment of osteoporosis due to the biological role of strontium, which has been found to reduce the incidents of fractures in osteoporotic patients. Administration of a suitable dose of Sr can promote bone formation and inhibit bone resorption, leading to enhanced bone mass and improved bone microarchitecture.[17,19−21] *In vitro* experiments have further disclosed that Sr has anabolic and anticatabolic activities, thus promoting collagen protein synthesis, enhancing osteoblast replication, and reducing osteoclast differentiation and osteoclast function.[21−28] Recently, it has been demonstrated that strontium can significantly down-regulate both the mRNA and protein levels of osteoblast-induced signals for osteoclastogenesis *via* the Ca^{2+} sensing receptor, thus positively affecting osteoblastic replication, differentiation, and lifespan.[27] Another recent report has suggested that Sr^{2+} acts *via* the Ca^{2+} sensing receptor to induce osteoclast apoptosis through a signaling pathway similar to but different in certain aspects from that of Ca^{2+}.[25] However, while a low dose of Sr benefits bone formation, high doses may pose deleterious effects on bone mineralization by decreasing calcium absorption and possibly altering the mineral properties.[29]

Generally, orally administered strontium cannot effectively reach the implant−tissue interface, particularly necrotic or avascular tissues left after surgery. This limitation can-

*Address correspondence to paul.chu@cityu.edu.hk, kfhuo@wust.edu.cn.

Received for review July 8, 2009 and accepted August 31, 2009.

Published online September 8, 2009. 10.1021/nn9007675 CCC: $40.75

not be overcome with increased doses due to organ toxicity associated with drugs at high concentrations. Oral administration will induce an increment of drug concentration in the blood plasma after intake, followed by a sinusoidal drop in the drug concentration with time. On the other hand, a controlled drug delivery system on the biomedical implants can offer a sustained complement of the element or drug. Therefore, a Sr releasing nanostructured surface on titanium implants not only exhibits favorable nanosize effects but also enables *in situ* Sr delivery to expedite osteointegration. The Sr loaded into the nanotubes is released to the implant−tissue interface locally and directly enabling effectively absorption by tissues in the vicinity, thereby promoting bone formation and suppressing bone resorption. This treatment is preferred over oral administration in osteoporotic patients. In comparison with Sr-containing hydroxyapatites (Sr-HAP) as bioactive coating materials,[29−32] TiO_2 nanotubes loaded with Sr that are grown directly on Ti implants have better mechanical performance. The requirements for slow but long-term release of Sr[19] preclude the use of direct loading of strontium-containing substances such as strontium ranelate or $SrCl_2$ or $Sr(OH)_2$ by solution chemistry. The good solubility of these substances will lead to fast leaching of Sr and a high Sr concentration in the vicinity.

In this paper, we report a novel method to accomplish sustained and controlled release of Sr. A bioactive $SrTiO_3$ nanotube array is produced on Ti implants by a simple hydrothermal treatment of an anodized titania nanotube array. The nanotubular effects which are retained by our technique promote attachment and growth of bone cell and also offer sustained release of Sr. Owing to weak dissolution, Sr is released slowly from the $SrTiO_3$ nanotubes at the implant−tissue interface for a long period of time. At the same time, the retained nanotube topography can be used for loading of other functional substances. That is, this method can be extended to load other trace elements such as Zn and Mg on Ti-based implants. This novel structure is projected to have immense potential in clinical medicine, especially osteoporotic bone implants.

RESULTS AND DISCUSSION

Structure Characterization. Titania nanotube arrays (TiO_2-NT) were produced by anodization of a chemically polished titanium plate. The titania nanotube arrays were subsequently subjected to a hydrothermal treatment in a $Sr(OH)_2$ solution, and well-ordered $SrTiO_3$ nanotube arrays (Sr-NT) were obtained. As shown in Figure 1, uniform nanotubes with a diameter of about 70 nm and length of about 1.3 μm can be produced by anodization. After the hydrothermal treatment, the original nanotube array architecture is retained as denoted in picture b in Figure 1. However, the diameter of the hydrothermally treated nanotubes decreases slightly, probably due to volume expansion during the

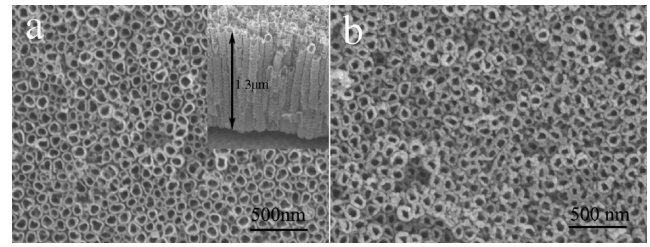

Figure 1. SEM micrographs of titania nanotube arrays and nanotube arrays after the hydrothermal treatment: (a) titania nanotube arrays and (b) nanotube arrays after hydrothermal treatment in $Sr(OH)_2$.

transformation from titanium oxide to strontium titanate. The X-ray diffraction (XRD) spectra in Figure 2 disclose the amorphous structure of the anodized titania naotubes. After the hydrothermal reaction, peaks from crystalline $SrTiO_3$ (cubic) can be observed. The hydrothermally treated nanotubes are heated to 450 °C for 3 h, and the anatase peaks emerge, implying that a part of the titanium oxide has not reacted as the residual amorphous titanium oxide turns into anatase after annealing. The structure of the $SrTiO_3$ nanotubes is further investigated by transmission electron microscopy (TEM), and the results are presented in Figure 3. By repeated sample binding, the nanotubes delaminate from the substrate and subsequent ultrasonic treatment in alcohol transports the nantube fragments from the sample surface into alcohol for the TEM investigation. The well-retained nanotube structure is verified in picture a. The structure of the Sr-NT is further evaluated by selected area diffraction (SAD). In order to exclude the influence of the amorphous carbon film on the copper grids, the SAD pattern (picture c) is obtained from another fragment at the hollow site shown in picture b. A polycrystalline diffraction pattern is observed from the $SrTiO_3$, and a diffusion pattern which is considered to arise from the amorphous titanium oxide is discerned. The results are in good agreement with the XRD spectra. Some ring-like fragments are also noted in picture d (denoted by arrows). These rings correspond to the top of the nanotube, and interestingly, the SAD patterns suggest a single-crystalline $SrTiO_3$ structure.

The Sr distribution along the nanotube is analyzed by X-ray photoelectron spectroscopy (XPS), and the results are displayed in Figure 4. A high Sr content is observed on the outermost surface, and the Sr concentration de-

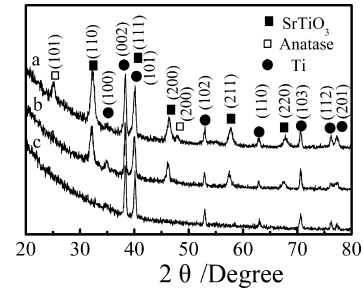

Figure 2. XRD patterns acquired from (a) $SrTiO_3$ nanotube arrays annealed at 450 °C for 3 h, (b) $SrTiO_3$ nanotube arrays, and (c) titania nanotube arrays.

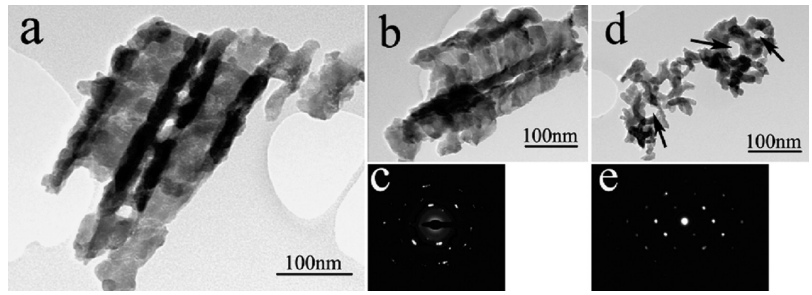

Figure 3. TEM views of the $SrTiO_3$ nanotube arrays and SAD pattern acquired from the selected region: (a) $SrTiO_3$ nanotube fragments; (b) $SrTiO_3$ nanotube fragments for SAD; (c) SAD pattern of fragments in picture b; (d) $SrTiO_3$ nanotube fragments; (e) SAD pattern in pictured.

creases with depth gradually. After about 80 min sputtering, nearly no Sr 3d signal can be detected, although a small amount of oxygen is still present. After sputtering for another 1 to 2 min, the O 1s peak cannot be detected. The results show that the hydrothermal reaction takes place on the entire anodized nanotube surface. The diminishing Sr concentration with depth is due to the insufficient hydrothermal reaction at deeper sites from the surface. Owing to the small diameter of the nanotubes, transportation or diffusion of reaction chemicals such as Sr^{2+} and OH^- from the outermost surface toward deeper sites is more difficult and thus the hydrothermal reaction is impeded. The Ti 2p high-resolution spectra after sputtering for 0, 2, 40, and 70 min are obtained to determine the chemical states. After sputtering for 2 min, only one set of doublet peaks (Ti $2p_{1/2}$ and Ti $2p_{3/2}$ centered at about 463.5 and 457.8 eV, respectively) corresponding to Ti in $SrTiO_3$[33] is observed. The spectra acquired after sputtering for 4 and 40 min show three other sets of doublet peaks ascribed to three chemical states of Ti: Ti^{2+}/TiO (Ti $2p_{1/2}$, 455.3 eV; Ti $2p_{3/2}$, 461.5 eV), Ti^{3+}/Ti_2O_3 (Ti $2p_{1/2}$, 457 eV; Ti $2p_{3/2}$, 463.1 eV), and Ti^{4+}/TiO_2 (Ti $2p_{1/2}$, 459.3 eV; Ti $2p_{3/2}$, 464.8 eV).[34,35] After sputtering for 70 min, peaks from pure Ti (Ti $2p_{1/2}$, 454.5 eV; Ti $2p_{3/2}$, 460.5 eV) emerge. According to the data, the top of the hydrothermally treated nanotubes contains only $SrTiO_3$ with a thickness of several tens of nanometers. Elemental depth profiles and Ti 2p fine spectra of the TiO_2-NT sample are also acquired as reference. The outermost surface contains a high content of O. The Ti and O signals are stable after

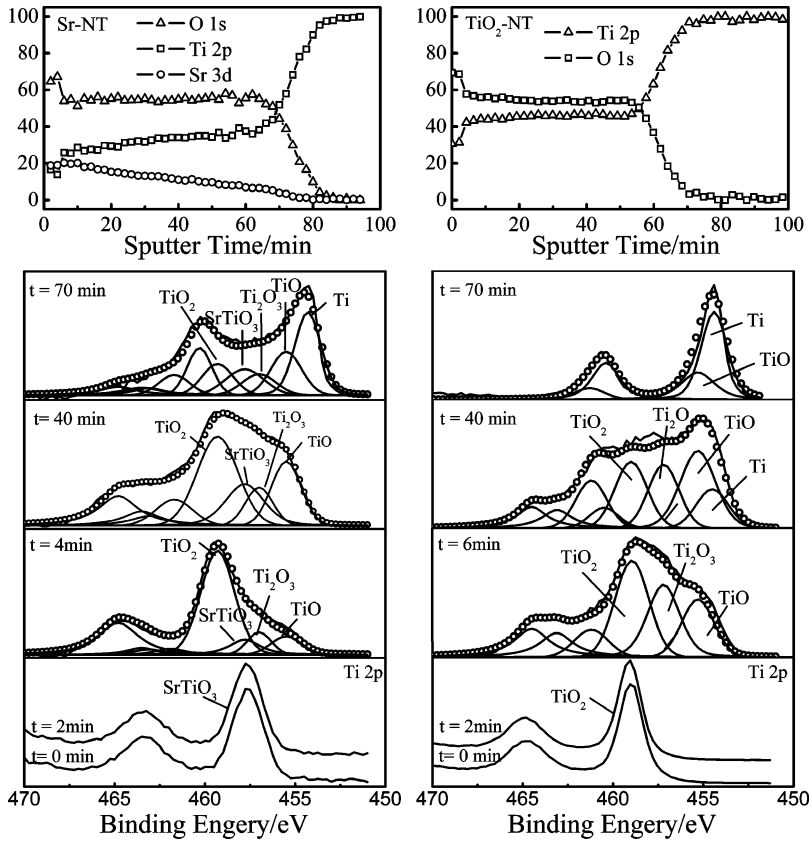

Figure 4. Elemental depth profiles acquired from the Sr-NT and TiO_2-NT samples by XPS and high-resolution Ti 2p spectra after different sputtering time (*t* represents the sputtering time, and the sputtering rate is approximately 21 nm/min referenced to SiO_2).

TABLE 1. Sr Release Rates from the $SrTiO_3$ Nanotube Arrays as a Function of Immersion Time in SBF

sample	2 weeks (μg/cm²)	4 weeks (μg/cm²)	loading efficiency (μg/cm²)
Sr-NT	5.3	8.5	60.5

about 6 min of sputtering time. Progressively increased Ti concentrations and quick drop in the O content are observed after about 58 min, which corresponds to the thickness of the barrier layer formed by anodization. The Ti 2p signal in the outermost surface only consists of one chemical state, Ti^{4+}/TiO_2. After sputtering for about 6 min, peaks corresponding to Ti^{2+}/TiO and Ti^{3+}/Ti_2O_3 also appear. When the sputtering time reaches about 70 min, a high Ti content exists together with a small amount of Ti^{2+}/TiO as shown in the spectrum. These XPS results further confirm that insufficient oxidization take place during anodization of pure titanium, and the as-anodized nanotubes consist of not only titania but also other forms of titanium oxide such as Ti_2O_3 and TiO.

Similar to the typical transformation from titanium oxide to titanate, the formation of $SrTiO_3$ also involves in a dissolution−precipitation process.[11,36,37] The Ti−O bonds on the TiO_2 precursor must be broken *via* hydrolytic attack to form soluble $[Ti(OH)_6]^{2-}$. This process is described below:

$$TiO_2 + 2OH^- + 2H_2O \rightarrow [Ti(OH)_6]^{2-} \quad (1)$$

Then, precipitation of $SrTiO_3$ takes place according to the following reaction:

$$Sr^{2+} + [Ti(OH)_6]^{2-} \rightarrow SrTiO_3 + 3H_2O \quad (2)$$

The total reaction is

$$TiO_2 + Sr(OH)_2 \rightarrow SrTiO_3 + H_2O \quad (3)$$

Dissolution of TiO_2 and precipitation of $SrTiO_3$ occur in the vicinity of the nanotube surfaces due to the absence of free $[Ti(OH)_6]^{2-}$ away from the area, and therefore, $SrTiO_3$ will preferentially nucleate at the nanotube surface. The $SrTiO_3$ layer formed in the beginning is loosely packed or porous and cannot totally block the transportation of Sr^{2+} and OH^-. After the reaction has elapsed for some time, a dense $SrTiO_3$ layer forms and transformation from TiO_2 to $SrTiO_3$ is consequently suppressed. Owing to the small diameter of the nanotubes, transportation or diffusion of Sr^{2+} and OH^- to the reaction sites away from the surface is more difficult, and hence, reaction 1 and then reaction 2 will be retarded. This leads to gradual decrease in the Sr concentration with depth as revealed by the XPS depth profiles.

Strontium Release. The loading efficiency (amount of Sr per 1 cm²) and release rate of Sr from the Sr-NT in simulated body fluids (SBF) free of Ca^{2+} are listed in Table 1. The use of Ca^{2+}-free SBF avoids the incorporation of Sr into the would-be precipitated hydroxyapatite, hence providing a more accurate assessment of the release rate because the $SrTiO_3$ nanotubes can induce the growth of hydroxyapatite in SBF (to be discussed later in this paper). The loading efficiency is about 60.5 μg/cm². During the first 2 weeks, 5.2 μg of Sr is released from 1 cm² of the surface, and in the subsequent 2 weeks, the release amount is about 3.3 μg/cm². The measured dissolution rates from $SrTiO_3$ have the same order of magnitude as that reported in ref 38. According to ref 38, Ti and Sr do not dissolve congruently. Sr can also be leached from the titanate matrix. Our data disclose continuous release of Sr from the Sr-NT at a slow rate. It has been reported that a Sr concentration on the order of μg/mL can induce obvious inhibition of bone resorption.[19] In our experiments, the release of Sr from the Sr-NT can introduce a local environment around the tissue and implant surface in which the Sr concentration has the magnitude of μg/mL. In addition, the nanotube length and diameter can be further tailored, for example, from several hundred nanometers to several hundred micrometers, and so the specific surface area can be

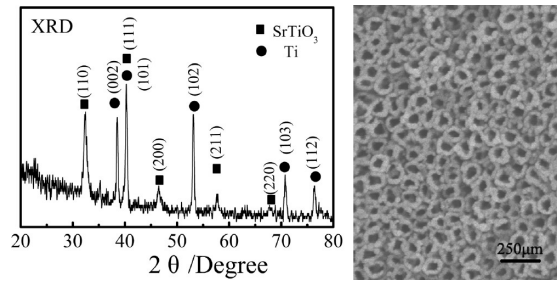

Figure 5. XRD spectrum and SEM picture of the Sr-NT sample after immersion in calcium-free SBF for 4 weeks.

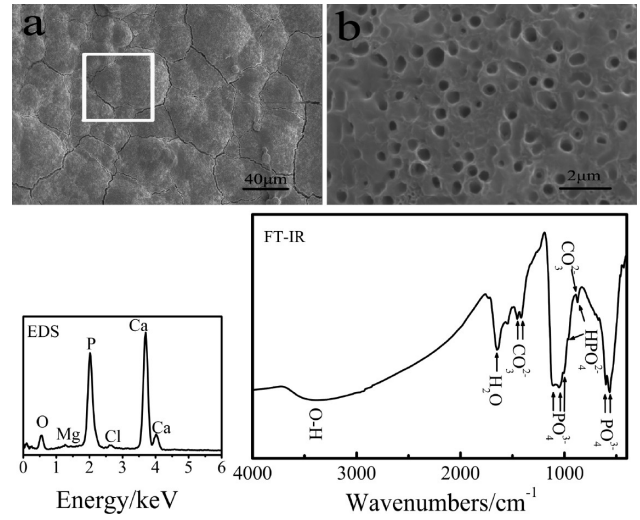

Figure 6. SEM views of the $SrTiO_3$ nanotube arrays after exposure to SBF for 28 days: (a) low-magnification views and (b) high-magnification views. The EDS results are acquired from the region in picture a indicated by the white rectangle. The FT-IR results are obtained from the $SrTiO_3$ nanotube arrays after immersion in SBF for 28 days.

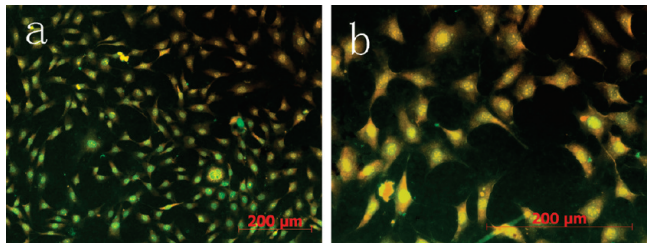

Figure 7. Cell morphology on the $SrTiO_3$ nanotube arrays after 5 days of culturing: (a) low magnification and (b) high magnification.

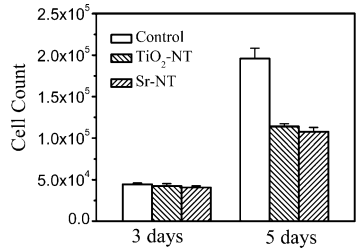

Figure 8. Cell numbers on the tissue plate, titania nanotube arrays, and $SrTiO_3$ nanotube arrays after culturing for 3 and 5 days.

adjusted to allow more flexible and controlled Sr release.[9,10]

The structure of the Sr-NT sample after exposure to Ca-ion-free SBF for 4 weeks is studied too, and the results are shown in Figure 5. The XRD spectrum discloses the existence of crystalline $SrTiO_3$. The SEM views indicate that the nanotube structure is well-retained after immersion. Obviously, leakage of Sr does not destroy the nanotube morphology.

Bioactivity and Biocompatibility. The ability to induce growth of hydroxyapatite in a physiological environment (usually named bioactivity or bone conductivity) is crucial for osteointegration of hard tissue implants. *In vitro* immersion experiments in SBF, which are usually performed to evaluate the bioactivity of biomaterials, have also been carried out in this work. After soaking in the SBF for 28 days, the Sr-NT surface is completely covered by a newly formed layer with round clusters, as depicted in Figure 6. The high magnification view reveals a porous structure. This precipitated layer contains large amounts of P, Ca, and O as well as trace amounts of Mg and Cl, as determined by energy dispersive X-ray spectroscopy (EDS) conducted at the selected region denoted by the white rectangle. In a physiological environment, Mg^{2+} and Na^+ ions may substitute for Ca^{2+} in the apatite and trace amounts of CO_3^{2-}, HPO_4^{2-}, F^-, and Cl^- may also be incorporated, leading to a nonstoichiometry composition of the apatite.[39] Here, the presence of Mg and Cl in the Ca−P-rich layer can be linked to the growth of biological apatite.

Fourier transform infrared spectroscopy (FT-IR) is employed to identify the functional groups in the precipitated layer, and the results are also presented in Figure 6. The broad absorption band from 3700 to 2500 cm^{-1} originates from the v_3 and v_1 stretching modes of hydrogen-bonded H_2O, and the band at 1650 cm^{-1} is ascribed to the v_2 binding mode of H_2O molecules.[40] The modes at 1420 (v_3) and 1450 (v_3) cm^{-1} arise from CO_3^{2-}.[41] A mode from HPO_4^{2-} is clearly discerned at the shoulder at 960 cm^{-1}, and thus the peaks at 876 cm^{-1} are the joint mode of $HPO_4^{2-}$and CO_3^{2-} (v_2). Bands from PO_4^{3-} (v_3) are found at 1000, 1050, and 1108 cm^{-1}.[6] According to Canham and co-workers,[42] a sharp bending mode doublet around 600 cm^{-1} is indicative of crystallized hydroxyapatite. Such binding modes of PO_4^{3-} are present at 576 and 601 cm^{-1}. According to the FT-IR results, the precipitated Ca−P-rich layer is composed of mainly hydroxyapatite. However, carbonate and HPO_4^{2-} are also incorporated into the apatite layer. The mechanism of HAP growth on crystalline $SrTiO_3$ is probably similar to that on crystalline $CaTiO_3$.[43] Similar to that proposed for $BaTiO_3$,[44] it is possible that $SrTiO_3$ can behave as insoluble TiO_2 and partially soluble SrO in the aqueous solution. Thus, the subtle dissolution of $SrTiO_3$ can be described as follows:

$$SrTiO_3 + H_2O \rightarrow Sr^{2+} + TiO_2 + 2OH^- \qquad (4)$$

The presence of negatively charged sites on TiO_2 at pH 7.42 attracts positively charged Ca^{2+} ions, followed by arrival of phosphate ions.[45] At the same time, generation of OH^- also enhances the pH value at the vicinity further promoting nucleation of HAP.

The *in vitro* biocompatibility of the Sr-NT is evaluated by cell adhesion and proliferation. The cell morphologies after 5 days are exhibited in Figure 7. The cells are observed to attach well onto the substrate and proliferate normally. The amounts of cells on the Sr-NT after 3 and 5 days of culturing are counted and compared to those on the TiO_2-NT and 24-well plate as control. In Figure 8, after 3 days, the cell numbers on all three substrates are similar. The cell number on the cultured tissue is highest among the three groups after 5 days, but the number of cells on the Sr-NT is close to that on the TiO_2-NT. It is well-known that titania has good biocompatibility,[4,5,8] and our results suggest that the $SrTiO_3$ nanotubes also possess biocompatibility comparable to that of titania nanotubes.

CONCLUSION

In summary, a Sr delivery platform is successfully fabricated on Ti-based implants by hydrothermal treatment of anodized titania nanotubes. Crystalline $SrTiO_3$ is obtained, and the nanotube topography is retained after the hydrothermal treatment. This $SrTiO_3$ nanotube array can release Sr at slow rate for a long time. *In vitro* experiments demonstrate that the $SrTiO_3$ nanotubes can induce precipitation of hydroxyapatite from simulated body fluids, and cell culture experiments indicate good biocompatibility of the nanotubes.

METHODS

Chemically polished pure titanium plates with dimensions of 20 mm × 10 mm × 1 mm were anodized in a solution (1 mol/L Na_2SO_4 + 0.1 mol/L NaF + 0.2 mol/L citric acid) for 20 h at a voltage 20 V. The anodized nanotubes underwent hydrothermal treatment in a $Sr(OH)_2$ solution. A series of hydrothermal treatments were conducted in the solution with various concentration of $Sr(OH)_2$ and at different temperature. The optimal nanotube structure was obtained in a 0.02 mol/L $Sr(OH)_2$ solution at 200 °C. Annealing was then conducted at 450 °C for 3 h, forming the three products: titania nanotubes (TiO_2-NT), $SrTiO_3$ nanotubes (Sr-NT), and annealed $SrTiO_3$ nanotubes (Sr-ANT).

X-ray diffraction (XRD, Cu Kα radiation, 40 kV, 30 mA) was employed to determine the structure of the samples. The pan views and cross-sectional views of the samples after gold coating were inspected by scanning electron microscopy (SEM, JEOL JSM-6335F). The structure of the Sr-NT sample was further studied using a Philips CM20 transmission electron microscope (TEM). The elemental distribution and chemical states were determined by X-ray photoelectron spectroscopy (XPS, Physical electronics, PH5802) with Al Kα excitation, 350 W power, and 45° taking off angle.

The Sr-NT samples were dissolved in a solution containing HF and HNO_3, and inductively coupled plasma emission spectrometry (ICP-ES) was utilized to measure the Sr concentrations by which the Sr loading efficiency was derived. The Sr-NT samples were immersed in SBF (free of Ca^{2+}) for a total 28 days to monitor the Sr release rate. The Sr concentrations were determined by ICP-ES, as well. Before immersion, the Sr-NT samples were ultrasonically rinsed in 0.1 mol mL HNO_3 for 3 min and distilled water for 1 h followed by soaking in distilled water for 2 days. This procedure was able to remove the residual $Sr(OH)_2$.

Biomimetic growth of hydroxyapatite on the Sr-NT was conducted by soaking the samples in SBF in which the ion concentrations are equal to those in human plasma. The SBF solution was prepared by dissolving reagent grade chemicals such as NaCl, KCl, $NaHCO_3$, $MgSO_4 \cdot 12\ H_2O_2$, $CaCl_2$, and K_2HPO_4 into doubly distilled water and buffered with tris-hydroxymethyl aminomethane and HCl at a pH of 7.4. The chemical composition is as follows (mmol/L): Na^+ = 142.0; K^+ = 5.0; Mg^{2+} = 1.0; Ca^{2+} = 2.5; Cl^- = 131.0; HCO_3^- = 5.0; HPO_4^- = 1.0; SO_4^{2-} = 1.0. The samples were immersed in 20 mL of SBF for 28 days at 37 °C, and the SBF was refreshed every 3 days. The samples were rinsed with distilled water after exposure to SBF.

The biocompatibility of the Sr-NT was assessed by cell culture experiments using Saos-2 cells. The tissue plate and TiO_2-NT were used as the control. The size of the samples used in the cell culture experiments was 8 mm × 8 mm × 1 mm. All of the samples were sterilized by 75% ethanol and rinsed with phosphate buffered saline (PBS) before cell seeding. The cells were cultured in a complete medium consisting of a mixture of 45% Dulbecco's Modified Eagle Medium (D-MEM) (Invitrogen cat no. 11995-040), 45% F-12 (Invitrogen cat no. 11765-047), and 10% fetal calf serum (FCS, Hyclone cat no. SV30087.02). They were maintained at 37 °C under 95% air and 5% CO_2. The subconfluent monolayers were dissociated with a 0.01% solution of trypsin and resuspended into a fresh complete medium. A 1000 μL complete culture medium containing about 5.0×10^3 cells was seeded on each sample. After 3 and 5 days, the samples were rinsed with PBS and fixed in methanol/acetic acid [9:1 (v/v)] for 20 min. The air-dried cells were then stained with 10 mg/mL acridine orange and observed under a fluorescence microscope. The cell morphology was recorded by a digital camera (Carl Zeiss Axioplan 2).

Acknowledgment. This work was financially supported by Hong Kong Research Grants Council (RGC) General Research Funds (GRF) No. CityU 112307, Key Project of Chinese Ministry of Education (No. 208087), Hubei Province Natural Science Foundation (No. ZRY0087), Key Grant Project of Educational Commission of Hubei Province of China (Z200711001), and National Natural Science Foundation of China (NSFC 50902104).

REFERENCES AND NOTES

1. Fini, M.; Giavaresi, G.; Torricelli, P.; Borsari, V.; Giardino, R.; Nicolini, A.; Carpi, A. Osteoporosis and Biomaterial Osteointegration. *Biomed. Pharmacother.* **2004**, *58*, 487–493.
2. Cai, Q. Y.; Paulose, M.; Varghese, O. K.; Grimes, C. A. The Effect of Electrolyte Composition on the Fabrication of Self-Organized Titanium Oxide Nanotube Arrays by Anodic Oxidation. *J. Mater. Res.* **2005**, *20*, 230–236.
3. Bayoumi, F. M.; Ateya, B. G. Formation of Self-Organized Titania Nano-Tubes by Dealloying and Anodic Oxidation. *Electrochem. Commun.* **2006**, *8*, 38–44.
4. Bauer, S.; Park, J. K.; von der Mark, K.; Schmuki, P. Improved Attachment of Mesenchymal Stem Cells on Super-Hydrophobic TiO_2 Nanotubes. *Acta Biomater.* **2008**, *4*, 1576–1582.
5. Popat, K. C.; Leoni, L.; Grimes, C. A.; Desai, T. A. Influence of Engineered Titania Nanotubular Surfaces on Bone Cells. *Biomaterials* **2007**, *28*, 3188–3197.
6. Tsuchiya, H.; Macak, J. M.; Müller, L.; Kunze, J.; Greil, P.; Vitanen, S.; Schmuki, P. Hydroxyapatite Growth on Anodic TiO_2 Nanotubes. *J. Biomed. Mater. Res., Part A* **2006**, *77A*, 534–541.
7. Popat, K. C.; Eltgroth, M.; LaTempa, T. J.; Grimes, C. A.; Desai, T. A. Decreased *Staphylococcus* Epidermis Adhesion and Increased Osteoblast Functionality on Antibiotic-Loaded Titania Nanotubes. *Biomaterials* **2007**, *28*, 4880–4888.
8. Brammer, K. S.; Oh, S. H.; Gallagher, J. O.; Jin, S. H. Enhanced Cellular Mobility Guided by TiO_2 Nanotube Surfaces. *Nano. Lett.* **2008**, *8*, 786–793.
9. Macak, J. M.; Tsuchiya, H.; Ghicov, A.; Yasuda, K.; Hahn, R.; Bauer, S.; Schmuki, P. TiO_2 Nanotubes: Self-Organized Electrochemical Formation, Properties and Applications. *Curr. Opin. Solid State Mater. Sci.* **2007**, *11*, 3–18.
10. Ghicov, A.; Schmuki, P. Self-Ordering Electrochemistry: A Review on Growth and Functionality of TiO_2 Nanotubes and Other Self-Aligned MO*x* Structures. *Chem. Commun.* **2009**, 2791–2808.
11. Wei, X. Z.; Vasiliev, A. L.; Padture, N. P. Nanotubes Patterned Thin Films of Barium−Strontium Titanate. *J. Mater. Res.* **2005**, *20*, 2140–2147.
12. Park, J.; Bauer, S.; von der Mark, K.; Schmuki, P. Nanosize and Vitality: TiO_2 Nanotube Diameter Directs Cell Fate. *Nano Lett.* **2007**, *7*, 1686–1691.
13. Park, J.; Bauer, S.; Schlegel, K. A.; Neukam, F. W.; von der Mark, K.; Schmuki, P. TiO_2 Nanotube Surfaces: 15 nm — An Optimal Length Scale of Surface Topography for Cell Adhesion and Differentiation. *Small* **2009**, *5*, 666–671.
14. Oh, S.; Jin, S. Titanium Oxide Nanotubes with Controlled Morphology for Enhanced Bone Growth. *Mater. Sci. Eng. C* **2006**, *26*, 1301–1306.
15. Popat, K. C.; Eltgroth, M.; La Tempa, T. J.; Grimes, C. A.; Desai, T. A. Titania Nanotubes: A Novel Platform for Drug-Eluting Coatings for Medical Implants. *Small* **2007**, *3*, 1878–1881.
16. Odabasi, E.; Turan, M.; Aydin, A.; Akay, C.; Kutlu, M. Magnesium, Zinc, Copper, Manganese, and Selenium Levels in Postmenopausal Women with Osteoporosis. Can Magnesium Play a Key Role in Osteoporosis? *Ann. Acad. Med. Singapore* **2008**, *37*, 564–567.
17. Nielsen, S. P. The Biological Role of Strontium. *Bone* **2004**, *35*, 583–588.
18. Zhang, D. W.; Cheng, Y.; Zhang, J. C.; Wang, X. L.; Wang, N. L.; Chen, Y.; Yang, M. S.; Yao, X. S. Synergistic Effect of Trace Elements and Flavonoids from Epimedium

Koreanum Nakai on Primary Osteoblasts. *Chin. Sci. Bull.* **2008**, *53*, 347–356.
19. Marie, P. J. Strontium Ranelate: a Novel Mode of Action Optimizing Bone Formation and Resorption. *Osteoporosis Int.* **2005**, *16*, S7–S10.
20. Ammann, P. Strontium Ranelate: A Novel Mode of Action Leading to Renewed Bone Quality. *Osteoporosis Int.* **2005**, *16*, S11–S15.
21. Marie, P. J. Strontium Ranelate: New Insights into its Dual Mode of Action. *Bone* **2007**, *4*, S5–S8.
22. Canalis, E.; Hott, M.; Deloffre, P.; Tsouderos, Y.; Marie, P. J. The Divalent Strontium Salt S12911 Enhances Bone Cell Replication and Bone Formation *In Vitro*. *Bone* **1996**, *18*, 517–523.
23. Capuccini, C.; Torricelli, P.; Sima, F.; Boanini, E.; Ristoscu, C.; Bracci, B.; Socol, G.; Fini, M.; Mihailescu, I. N.; Bigi, A. Strontium-Substituted Hydroxyapatite Coatings Synthesized by Pulsed-Laser Deposition: *In Vitro* Osteoblast and Osteoclast Response. *Acta Biomater.* **2008**, *4*, 1885–1893.
24. Bonnelye, E.; Chabadel, A.; Saltel, F.; Jurdic, P. Dual Effect of Strontium Ranelate: Stimulation of Osteoblast Differentiation and Inhibition of Osteoclast Formation and Resorption *In Vitro*. *Bone* **2008**, *42*, 129–138.
25. Hurtel-Lemaire, A. S.; Mentaverri, R.; Caudrillier, A.; Cournarie, F.; Wattel, A.; Kamel, S.; Terwilliger, E. F.; Brown, E. M.; Brazier, M. The Calcium-Sensing Receptor is Involved in Strontium Ranelate-Induced Osteoclast Apoptosis. *J. Biol. Chem.* **2009**, *284*, 575–584.
26. Peng, S. L.; Zhou, G. Q.; Luk, K. D. K.; Cheung, K. M. C.; Li, Z. Y.; Lam, W. M.; Zhou, Z. J.; Lu, W. W. Strontium Promotes Osteogenic Differentiation of Mesenchymal Stem Cells through the Ras/MAPK Signaling Pathway. *Cell Physiol. Biochem.* **2009**, *23*, 165–174.
27. Brennan, T. C.; Rybchyn, M. S.; Green, W.; Atwa, S.; Conigrave, A. D.; Mason, R. S. Osteoblasts Play Key Roles in the Mechanisms of Action of Strontium Ranelate. *Br. J. Pharmacol.* **2009**, *157*, 1291–1300.
28. Fromigué, O.; Haÿ, E.; Barbara, A.; Petrel, C.; Traiffort, E.; Ruat, M.; Marie, P. J. Calcium Sensing Receptor-Dependent and -Independent Activation of Osteoblast Replication and Survival by Strontium Ranelate. *J. Cell Mol. Med.* **2009**, 19187125.
29. Ni, G. X.; Lu, W. W.; Xu, B.; Chiu, K. Y.; Yang, C.; Li, Z. Y.; Lam, W. M.; Luk, K. D. K. Interfacial Behaviour of Strontium-Containing Hydroxyapatite Cement with Cancellous and Cortical Bone. *Biomaterials* **2006**, *27*, 5127–5133.
30. Ni, G. X.; Chiu, K. Y.; Lu, W. W.; Wang, Y.; Zhang, Y. G.; Hao, L. B.; Li, Z. Y.; Lam, W. M.; Lu, S. B.; Luk, K. D. K. Strontium-Containing Hydroxyapatite Bioactive Bone Cement in Revision Hip Arthroplasty. *Biomaterials* **2006**, *27*, 4348–4355.
31. Landi, E.; Tampieri, A.; Celotti, G.; Sprio, S.; Sandri, M.; Logroscino, G. Sr-Substituted Hydroxyapatites for Osteoporotic Bone Replacement. *Acta Biomater.* **2007**, *3*, 961–969.
32. Guo, D. G.; Xu, K. W.; Han, Y. The Influence of Sr Doses on the *In Vitro* Biocompatibility and *In Vivo* Degradability of Single-Phase Sr-Incorporated HAP Cement. *J. Biomed. Mater. Res., Part A* **2008**, *88A*, 947–958.
33. Ehre, D.; Cohen, H.; Lyahovitskaya, V.; Lubomirsky, I. X-ray Photoelectron Spectroscopy of Amorphous and Quasiamorphous Phases of $BaTiO_3$ and $SrTiO_3$. *Phys. Rev. B* **2008**, *77*, 184106.
34. Tan, L.; Crone, W. C. Surface Characterization of NiTi Modified by Plasma Source Ion Implantation. *Acta Mater.* **2002**, *50*, 4449–4460.
35. Chu, C. L.; Hu, T.; Wu, S. L.; Dong, Y. S.; Yin, L. H.; Pu, Y. P.; Lin, P. H.; Chung, C. Y.; Yeung, K. W. K.; Chu, P. K. Surface Structure and Properties of Biomedical NiTi Shape Memory Alloy after Fenton's Oxidation. *Acta Biomater.* **2007**, *3*, 795–806.
36. Qi, L.; Lee, B. I.; Badheka, P. B.; Yoon, D. H.; Samuels, W. D.; Exarhos, G. J. Short-Range Dissolution-Precipitation Crystallization of Hydrothermal Barium Titanate. *J. Eur. Ceram. Soc.* **2004**, *24*, 3553–3557.
37. Eckert, J. O.; HungHouston, C. C.; Gersten, B. L.; Lencka, M. M.; Riman, R. E. Kinetics and Mechanisms of Hydrothermal Synthesis of Barium Titanate. *J. Am. Ceram. Soc.* **1996**, *79*, 2929–2939.
38. Anderson, J.; Kahn, B.; LaBone, T.; Brown, L.; Harris, F. Solubility of Various Forms of Strontium Titanate in Lungs: *In Vitro* and *In Vivo* Studies. *Health Phys.* **1999**, *76*, 628–634.
39. Lowenstam, H. A.; Weiner, S. *On Biomineralizatin*; Oxford University Press: Oxford, 1989.
40. Jevtic, M.; Mitric, M.; Skapin, S.; Jancar, B.; Ignjatovic, N.; Uskokovic, D. Crystal Structure of Hydroxyapatite Nanorods Synthesized by Sonochemical Homogeneous Precipitation. *Cryst. Growth Des.* **2008**, *8*, 2217–2222.
41. Weng, J.; Liu, Q.; Wolke, J. G. C.; Zhang, X. D.; deGroot, K. Formation and Characteristics of the Apatite Layer on Plasma-Sprayed Hydroxyapatite Coatings in Simulated Body Fluid. *Biomaterials* **1997**, *18*, 1027–1035.
42. Canham, L. T.; Reeves, C. L.; Loni, A.; Houlton, M. R.; Newey, J. P.; Simons, A. J.; Cox, T. I. Calcium Phosphate Nucleation on Porous Silicon: Factors Influencing Kinetics in Acellular Simulated Body Fluids. *Thin Solid Films* **1997**, *297*, 304–307.
43. Coreno, J.; Coreno, O. Evaluation of Calcium Titanate as Apatite Growth Promoter. *J. Biomed. Mater. Res., Part A* **2005**, *75A*, 478–484.
44. Lopez, M. C. B.; Rand, B.; Riley, F. L. The Isoelectric Point of $BaTiO_3$. *J. Eur. Ceram. Soc.* **2000**, *20*, 107–118.
45. Takadama, H.; Kim, H. M.; Kokubo, T.; Nakamura, T. An X-ray Photoelectron Spectroscopy Study of the Process of Apatite Formation on Bioactive Titanium Metal. *J. Biomed. Mater. Res.* **2001**, *55*, 185–193.